Improved catalytic efficiency and stability by surface activation in Fe-based amorphous alloys for hydrogen evolution reaction in acidic electrolyte

Genmiao Shao[a], Qianqian Wang[a], Fang Miao[a], Jiaqi Li[a], Yongjie Li[a], Baolong Shen[a,b,*]

[a] School of Materials Science and Engineering, Jiangsu Key Laboratory for Advanced Metallic Materials, Southeast University, Nanjing 211189, China
[b] Institute of Massive Amorphous Metal Science, China University of Mining and Technology, Xuzhou 221116, China

ARTICLE INFO

ABSTRACT

The development of efficient and durable electrocatalysts for water splitting to produce hydrogen is of great significance to relieve the energy crisis. In this work, a self-supported FeMoPC amorphous catalyst with a sandwich structure prepared by the electrochemical activation-dealloying two-step method is reported. The catalyst exhibits a low overpotential of 96 mV at -10 mA cm^{-2}, a Tafel slope of 51 mV dec^{-1}, and excellent stability for over 16 h in 0.5 M H_2SO_4 solution for hydrogen evolution reaction (HER). The good catalytic activity is attributed to the nanoislands with rich active sites and large reaction areas for efficient HER obtained by an electrochemical cyclic voltammetry scan activation. Additionally, the formation of a compact protective phosphate/oxide layer that has high concentration of Mo on the surface during the subsequent dealloying enhances the durability of the catalyst. This work overcomes the issues associated with poor durability of Fe-based catalyst in acidic electrolyte and broadens the application of Fe-based amorphous alloys.

1. Introduction

The energy and environment crises have urged the development of hydrogen production technologies. Compared with other technologies, the electrochemical water splitting is regarded as the most promising approach to produce hydrogen as it has zero carbon emission and high purity of products [1-4]. The hydrogen evolution reaction (HER), which is an important half-reaction involved in water splitting, is kinetically not favored and requires catalysts to accelerate the reaction rate [5,6]. Up to now, the commercial HER catalysts are mainly noble metals, including Pt and Pd, and their scarcity makes them high cost [7-11]. Thus, it is important to develop earth-abundant materials based high-performance catalysts.

Recent researches prove that transition metals (e.g., Fe, Co and Ni) based carbides [12,13], nitrides [14-16], phosphides [17-23] and sulfides [24,25] exhibit superior HER catalytic activity, as the incompletely filled *d* orbitals of transition metals are benefit for electron transportation [26-28]. Furthermore, compared with crystalline materials, amorphous counterparts have more advantages as

catalysts. The long-range disordered atomic arrangement in amorphous materials leads to abundant active sites, as well as the good corrosion resistance that makes the catalyst durable [29-34]. In comparison to powdery catalysts, the amorphous ribbons prepared by melt spinning are ductile and self-supported, which are more suitable for industrial applications [35,36].

Among all the transition metal-based amorphous ribbons for HER catalysts, Fe-based amorphous alloy are considered as the promising candidates due to their diverse alloy composition, low materials cost and excellent HER properties [37]. For example, $Fe_{40}Co_{40}P_{13}C_7$ amorphous ribbons have been found to exhibit superior HER ability attributed to a combination of the metastable state and the synergetic effect of elements [38]. Similarly, the ultrasonic vibration treated $Fe_{78}Si_9B_{13}$ amorphous ribbons with enlarged electrochemical active area and higher atomic energy, can serve as an efficient HER catalyst [39]. However, as Fe-based catalysts have relatively low corrosion resistance in acidic electrolyte, their durability for HER catalysis is far from satisfactory. For example, $Fe_{80}P_{13}C_7$ amorphous ribbons show a very low overpotential in acidic electrolyte, but exhibits a percentage of 80% drop in current density after 2 h HER test [38]. Considering that water electrolysis based on proton exchange membrane (PEM) technology operates under strong acidic conditions [40], improving the durability of Fe-based catalysts while maintaining their high catalytic activity is

---

crucial for application as HER catalysts. The durability of Fe-based catalysts can be improved by alloying with corrosion-resistant elements, such as Mo. Besides, transition metals, including Fe, Co and Ni, possess low hydrogen adsorption free energies (ΔG_H) close to the vertex of the volcano plot according to the Sabatier principle, while Mo possesses strong ΔG_H [41]. Alloying of Mo with transition metals leads to a moderate metal−hydrogen bond energy (E_{M-H}), which can accelerate the hydrogen evolution reaction. Many studies about the positive effect of Mo alloying on transition metal based amorphous materials as HER catalyst have been reported, such as np-NiMoO amorphous ribbons [42] and electrodeposited CoMoPO amorphous film [43]. However, the effect of Mo alloying in the HER performance of Fe-based amorphous catalysts has not been investigated.

Furthermore, other than composition modulation, increasing the relative surface area by constructing specific surface structure is also an effective strategy to optimize the catalytic activities for some bulk electrodes [44,45]. Cyclic voltammogram scan activation (CV-activation) and dealloying in acidic solutions are common methods for surface modification. The HER performance of $Pd_{40}Ni_{10}Cu_{30}P_{20}$ amorphous ribbons is significantly enhanced with formation of localized Pd and Cu element groups on the surface by CV-activation [9]. The nanoporous NiFePB amorphous ribbons were obtained by dealloying, and exhibit good catalytic activity and long-term stability [46]. The combination of CV-activation and dealloying may have the synergetic effect on the surface morphology, and thus affect the electrochemical performance of the catalysts.

In this work, Mo element was introduced in FePC amorphous alloys to produce FeMoPC amorphous ribbons as self-supported HER catalysts, and the Fe/Mo ratio was adjusted to optimize the catalytic activity and durability. A two-step surface treatment with CV-activation followed by dealloying was adopted to improve the electrochemical performance of the amorphous ribbons. The $Fe_{76}Mo_4P_{13}C_7$ amorphous ribbons with nanoisland structures on the surface exhibit a low overpotential of 96 mV at 10 mA cm^{-2}, a small Tafel slope of 51 mV dec^{-1} and excellent long-term stability for over 16 h in 0.5 M H_2SO_4 electrolyte, which are comparable to that of some noble metal-based catalysts. This work presents an effective approach to enhance activity and durability of Fe-based catalysts through composition modulation and surface treatment.

2. Experimental

2.1. Materials preparation

The $Fe_{80-x}Mo_xP_{13}C_7$ (x = 4, 10 at%) alloy ingots were prepared by arc melting the high-purity (>99.90%) Fe, Mo, C first and then induction melting Fe_3P, FeMoC alloy under argon atmosphere. Ribbons with a thickness of 22 μm and a width of 1.5 mm were prepared in a single roller melt-spinning system, which was vacuumed to 5×10^{-3} Pa first and then filled with high-purity argon (99.999%). The ribbon keeps a relatively high tensile strength of 878 MPa, as shown in Fig. S1. The ribbons were then cut into 2 cm long for the electrocatalytic measurements. The electrochemical CV activation was performed by a continuous CV scan at a scan rate of 10 mV s^{-1} from -0.19 to 0.16 V (vs. RHE) until CV scan curves were stabilized, as shown in Fig. S2. Dealloying of ribbons before and after the CV-activation was carried out in 9.6 M HNO_3 solutions at room temperature for 20 min, followed by washing with deionied water. The as-spun, CV-activated only, dealloyed only, and CV-activated plus dealloyed $Fe_{80-x}Mo_xP_{13}C_7$ (x = 4, 10 at%) ribbons are labeled as As-spun Mox, CV Mox, DE Mox and DE@CV Mox (x = 4, 10), respectively.

2.2. Materials characterizations

The amorphous structures of samples were verified by X-ray diffraction (XRD, D8-Discover) with Cu-Kα radiation. The atomic structure of the As-spun Mo4 was characterized by transmission electron microscopy (TEM, JEM-2100F). The atomic structure and element mappings of the DE@CV Mo4 were characterized by TEM (Tecnai G2 F30) equipped with energy dispersive x-ray analysis (EDAX). The surface morphology and element information of samples were observed by scanning electron microscopy (SEM, FEI Inspect F50) equipped with energy dispersive X-ray spectrometer (EDS). The binding states of elements on the surfaces of samples were evaluated by X-ray photoelectron spectroscopy (XPS, Thermo Fisher Nexsa) using the Al-Kα X-ray ($h\nu$ = 1486.6 eV) source with a pass energy of 150.0 eV, a step size of 1.0 eV, a dwell time of 50 ms and a spot size of 400 μm.

2.3. Electrochemical measurements

The electrochemical measurements were conducted in 0.5 M H_2SO_4 solution using an electrochemical workstation (Gamry Interface 1000) with a three-electrode system. The carbon rod and Ag/AgCl serve as counter electrode and reference electrode, respectively. Ribbons were used as working electrode with the working area of 0.3 cm^2 (1.5 mm*10 mm*2). Commercial Pt/C nanopowders (Pt 20% Johnson Matthey) were used as a control electrode. The preparation method of Pt/C electrode was as follows: Firstly, 4 mg catalyst with ethanol/water (1000 μL, 3:1) and 15 μL Nafion (5 wt%, DuPont) solution were mixed under ultrasonication for 1 h. Then 5 μL droplets were loaded on a polished glass carbon electrode (3 mm in diameter) and dried at room temperature. The Ag/AgCl was calibrated by referring to the reversible hydrogen electrode (RHE, Phychemi) according to the following steps: Firstly, the RHE was immersed in 0.5 M H_2SO_4 solution for 2 h before use. Then, the open circuit voltage measurement was performed in 0.5 M H_2SO_4 solution using the electrochemical workstation with a two-electrode system. The RHE and Ag/AgCl serve as the reference electrode and working electrode, respectively. Finally, the potential value was recorded when the open circuit potential reached a steady state. The relative potential of Ag/AgCl vs. RHE measured in 0.5 M H_2SO_4 solution is -208 mV. All potentials were converted to the reversible hydrogen potential according to the Nernst equation. Linear scan voltammetry (LSV) was conducted at a potential sweep rate of 5 mV s^{-1}. The Tafel slopes of the catalysts were determined by the linear region of LSV polarization curves. The electrochemical impedance spectroscopy (EIS) was measured at open-circuit potential with scanning frequencies from 100 kHz to 0.01 Hz and AC voltage amplitude being 10 mV. All measured potentials were compensated by *iR* with the solution resistance obtained from the EIS measurements. The double-layer capacitance (C_{dl}) was estimated by CV at sweep rates of 10, 20, 30, 40 and 50 mV s^{-1}. When the capacitive current densities ($\Delta j = j_{anodic} - j_{cathodic}$) and the scan rates were linearly fitted, the slope was twice the double-layer capacitance (C_{dl}). The electrochemical active surface area (ECSA) was calculated by C_{dl}/C_s, where C_s is the specific capacitance and the value is 0.035 mF cm^{-2} [47]. To evaluate the stability of the catalysts, the chronopotentiometry (CP) tests were recorded at a current density of 10 mA cm^{-2}.

3. Results and discussion

The preparation process of DE@CV Mo4 is shown in Scheme 1. Ductile ribbons (As-spun Mo4) were prepared by rapid quenching, followed by CV-activation and then dealloying. Nanoisland structures were formed on the surface after CV-activation, then the
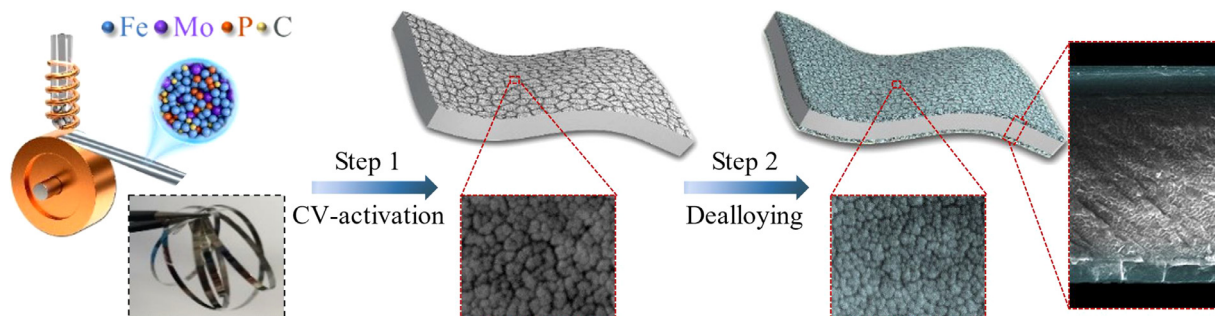
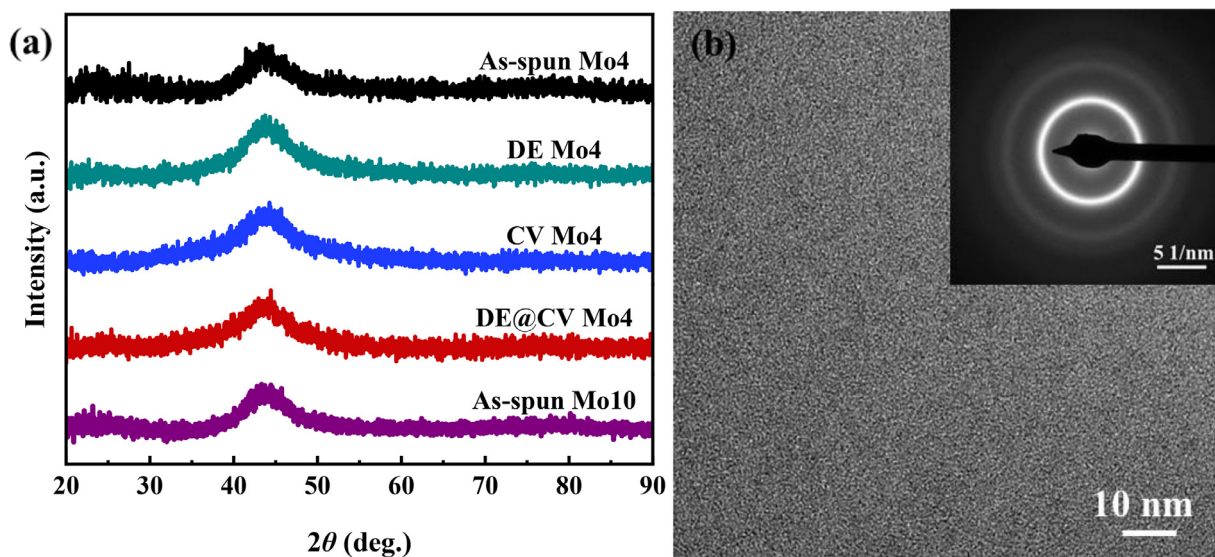**Scheme 1.** Illustration of the preparation process of the DE@CV Mo4.

Fig. 1. (a) XRD patterns of the As-spun Mo4, DE Mo4, CV Mo4, DE@CV Mo4 and As-spun Mo10, (b) HRTEM image of the As-spun Mo4.

dealloying treatment reduces the size of nanoislands while enhances the thickness of the nanoisland layers on both surfaces. A sandwich-like structure with nanoisland layer on the surfaces was then formed. Details about the structure of the samples will be discussed in later parts.

The amorphous structures of the prepared samples were confirmed by XRD. As shown in Fig. 1a, the XRD patterns only exhibit a broad diffraction peak (about 44°), indicating all of the ribbons are composed of an amorphous phase only. To further verify the amorphous nature of the ribbons, the high-resolution TEM (HRTEM) analysis of the As-spun Mo4 was carried out as a representative, as shown in Fig. 1b. No long-range ordered atomic arrangements, such as lattice fringes, are observed in the HRTEM image, and no diffraction dots appears in the SAED pattern, as shown in the inset. These results confirm the amorphous structure of the ribbons down to nanoscale.

To evaluate the concentration of Mo on the HER catalytic activity, the electrochemical measurements of the As-spun Mo4 and Mo10 were carried out in 0.5 M H_2SO_4 using a standard three-electrode system. The *iR*-corrected LSV curves are shown in Fig. 2a and Fig. S3a. The overpotential (η) needed for As-spun Mo4 to reach a current density of 10 mA cm^{-2} is 165 mV, which is much lower than 286 mV for the As-spun Mo10, indicating that the excessive addition of Mo reduces intrinsic catalytic activity of Fe-based amorphous alloys. This can be explained by the strong hydrogen binding energy of Mo [5].

Based on the above-mentioned results, the As-spun Mo4 was treated by CV-activation, dealloying and CV-dealloying to enhance

its catalytic performance. Fig. 2a shows the LSV curves of Mo4 ribbons in the different treated states. At the current density of 10 mA cm^{-2}, the DE@CV Mo4 exhibits the low overpotential ($\eta_{10} = 96$ mV), which is close to that of the CV Mo4 ($\eta_{10} = 90$ mV) and much lower than that of the DE Mo4 ($\eta_{10} = 126$ mV). The overpotential of the CV Mo4 and DE@CV Mo4 are even smaller than the reported noble metal-based HER catalysts, such as IrNiTa/Si ($\eta_{10} = 99$ mV) [48], and Pt@PCM ($\eta_{10} = 105$ mV) [49]. For comparison, the performances of the DE@CV Mo10 was also evaluated, the η_{10} is found to be 154 mV (Fig. S3a). The HER kinetics was estimated by Tafel plots. As shown in Fig. 2b, the Tafel slope of the DE@CV Mo4 is 51 mV dec^{-1}, which is smaller than that of the CV Mo4 (55 mV dec^{-1}), As-spun Mo4 (56 mV dec^{-1}) and the reported $Pd_{40}Ni_{10}Cu_{30}P_{20}$ (58 mV dec^{-1}) [9]. The smaller Tafel slope implies the faster HER rate, thus DE@CV Mo4 has a superior HER catalytic performance. The Tafel slope is also used to analyze the HER mechanism (Volmer-Heyrovsky or Volmer-Tafel). The HER is a two-step progress in acidic solutions. The first step of the HER is the Volmer reaction ($H_3O^+ + e^- + M \rightarrow MH_{ads} + H_2O$), the second step is either the Heyrovsky reaction ($MH_{ads} + e^- + H^+ \rightarrow M + H_2$) or Tafel reaction ($2MH_{ads} \rightarrow 2M + H_2$), and M denotes the active site. The corresponding Tafel slopes of the Tafel, Heyrovsky, and Volmer reactions are 30, 40, and 120 mV dec^{-1}, respectively. As the measured Tafel slope for the DE@CV Mo4 is 51 mV dec^{-1}, the HER process catalyzed by the DE@CV Mo4 follows the Volmer-Heyrovsky mechanism.

To further understand the HER process catalyzed by the FeMoPC ribbons, the interfacial properties and reaction kinetics of the cat-
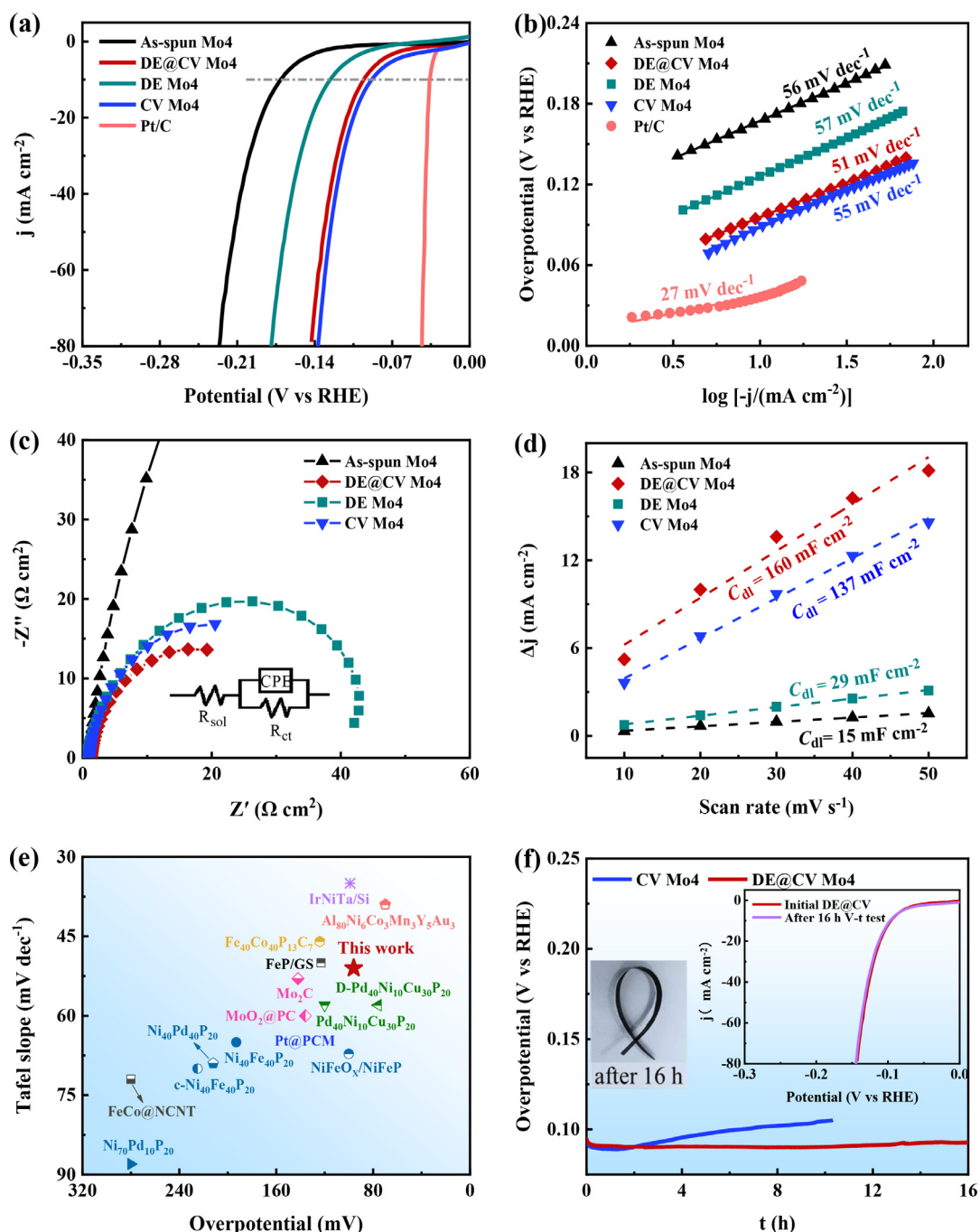
Fig. 2. Electrocatalytic property measurements of the As-spun Mo4, DE Mo4, CV Mo4, DE@CV Mo4 and Pt/C catalysts in 0.5 M H_2SO_4 electrolyte, (a) HER polarization curves measured at 5 mV s^{-1}, (b) Corresponding Tafel slopes of the samples, (c) EIS curves measured at open-circuit potential, (d) Current density differences at -0.03 V (vs RHE) plotted against the scan rate. (e) Comparison of the HER activities with representative previously reported HER electrocatalysts in acidic solutions. (f) Stability tests of the CV Mo4 and DE@CV Mo4 under static current density of 10 mA cm^{-2}, the insets are LSV curves of the DE@CV Mo4 before and after 16 h HER test, and the photograph of the DE@CV Mo4 ribbon after 16 h HER test.

alysts were evaluated by EIS. In general, the reaction rate of the catalysts is controlled by the charge transfer resistance (R_{ct}), and a lower R_{ct} means a faster reaction rate. Fig. 2c shows the Nyquist plots of the ribbons at different treated states obtained from the EIS, and the plots are fitted using an equivalent circuit model (inset of Fig. 2c). The R_{ct} of the As-spun Mo4 ribbons is sharply reduced from 362 Ω cm^2 to 39 Ω cm^2 after the CV-activation, and then decreases slightly to 32 Ω cm^2 after the subsequent dealloying. As shown in Fig. S3c, the R_{ct} of the DE@CV Mo10 is also obviously lower than that of the As-spun Mo10. The lower R_{ct} values

of the CV Mo4 and DE@CV Mo4 indicate their better charge transfer ability, which is beneficial to improve electrocatalytic hydrogen evolution activity.

To study the effect of the CV-activation and dealloying on the electrochemical active surface area (ECSA), the double-layer capacitance (C_{dl}), was estimated by cyclic voltammetry (CV) at different sweep rates (Fig. S4), and the values of C_{dl} are summarized in Fig. 2d. Impressively, the C_{dl} of the CV Mo4 is 137 mF cm^{-2}, which is significantly higher than of the DE Mo4 (29 mF cm^{-2}) and As-spun Mo4 (15 mF cm^{-2}). After further dealloying the CV-activated
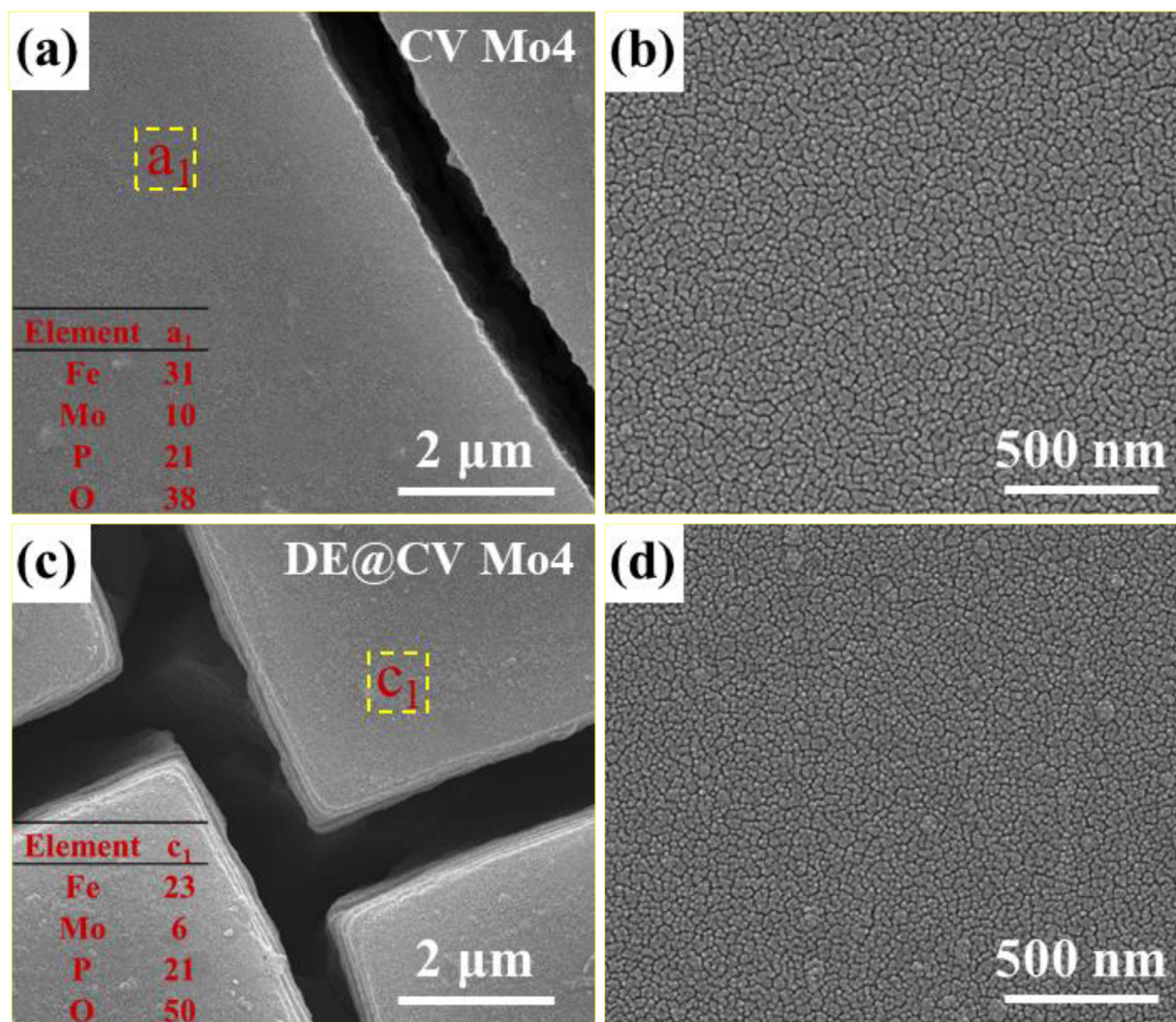
Fig. 3. SEM images of (a, b) the CV Mo4 and (c, d) the DE@CV Mo4 at different magnifications.

ribbons, the DE@CV Mo4 shows an even larger C_{dl} of 160 mF cm^{-2}. The greatly increased ECSA of the CV Mo4 indicates that amounts of active sites were produced on the surface of Mo4 ribbons during the CV cycling. Based on the results of the EIS and ECSA, the reduced charge transfer resistance and the increased abundant active sites contribute to the lower overpotential values of the CV-activated and DE@CV samples.

The values of overpotential and Tafel slope for the DE@CV Mo4 are compared with previously reported catalysts in acidic solutions, including Fe, Pd, Ni-based amorphous ribbons, alloys, carbide, oxides and other noble metal, as shown in Fig. 2e. The detailed electrochemical properties and testing parameters of the catalysts are listed in Tab. S1. The DE@CV Mo4 exhibits both the low overpotential and Tafel slope, which is superior to most of the reported non-noble and noble metal-based catalysts.

The durability of HER catalysts is another key parameter for industrial applications. The long-term stability of the CV Mo4 and DE@CV Mo4 were examined by chronopotentiometry at a constant current density of 10 mA cm^{-2}. As shown in Fig. 2f, the overpotential of the CV Mo4 increases from 88 to 118 mV after 10 h test, suggesting that its durability is far from satisfactory. In comparison, the DE@CV Mo4 exhibits superior durability, its overpotential has lesser increase after 16 h test. The stability of the DE@CV Mo4 was also evaluated by measuring the LSV curves before and after the 16 h chronoamperometry measurement, with the results shown in

the inset of Fig. 2f. No obvious change of the LSV curves can be observed, and the R_{ct} of the DE@CV Mo4 is still as low as 36 Ω cm^2 (Fig.S5), which further indicates that the dealloying would promote the durability of the CV-activated ribbons. Besides, the DE@CV Mo4 ribbon maintains good ductility even after 16 h test, as shown by the photograph in the inset of Fig. 2f.

In order to uncover the origin of the improved catalytic activity after the CV-activation and the enhanced durability after dealloying, the surface morphology of the catalysts was analyzed. As shown in Fig. 3a, the SEM image of the CV Mo4 reveals a cracked morphology due to the generated/released stress between the surface layer and the underlaid matrix. Fig. 3b shows that the surface of the CV Mo4 is formed of abundant nanoislands with a size of ~70 nm, originating from the dissolution of iron atoms during the CV-activation. The nanoislands would enlarge the specific surface area, facilitating mass transfer and desorption of the produced gaseous H$_2$ to achieve low charge transfer resistance, and thus accelerate the HER process. As shown in Fig. 3c and d, the DE@CV Mo4 exhibits an obvious hierarchical structure and keeps the similar nanoisland structures to the CV Mo4, but with a smaller size of ~50 nm, which are responsible for the increase of specific surface area.

As shown in Fig. 4a and c, the cross-sectional SEM images of the DE@CV Mo4 show a sandwich-like structure with a ~2 μm thick porous layer on the surface, which is different from that of
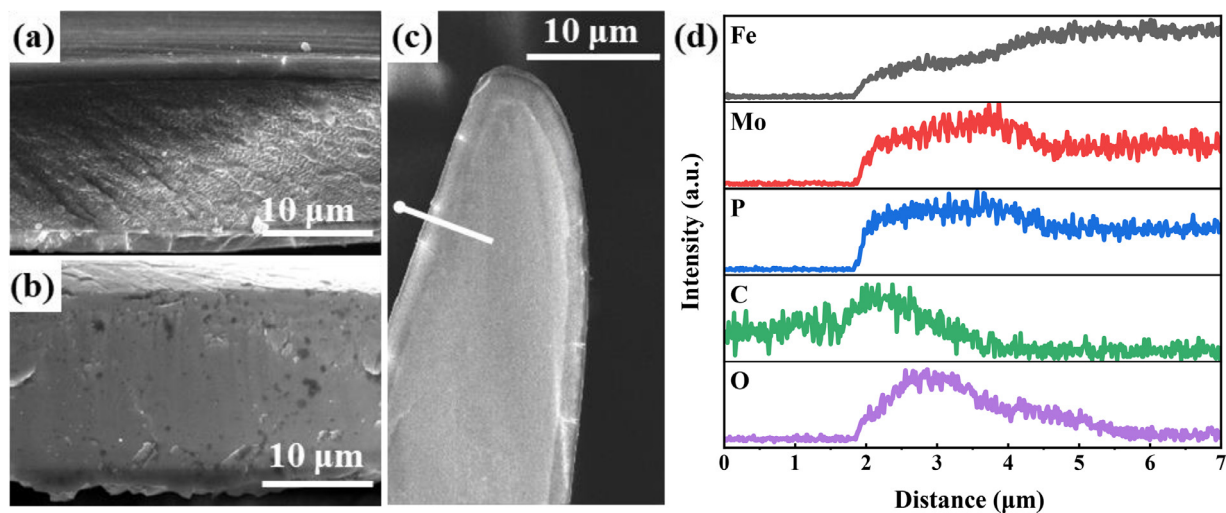
Fig. 4. Cross-section morphology of (a) the DE@CV Mo4, (b) the CV Mo4, and (c) the edge of DE@CV Mo4, (d) the corresponding EDS line scan results of the white line in (c).
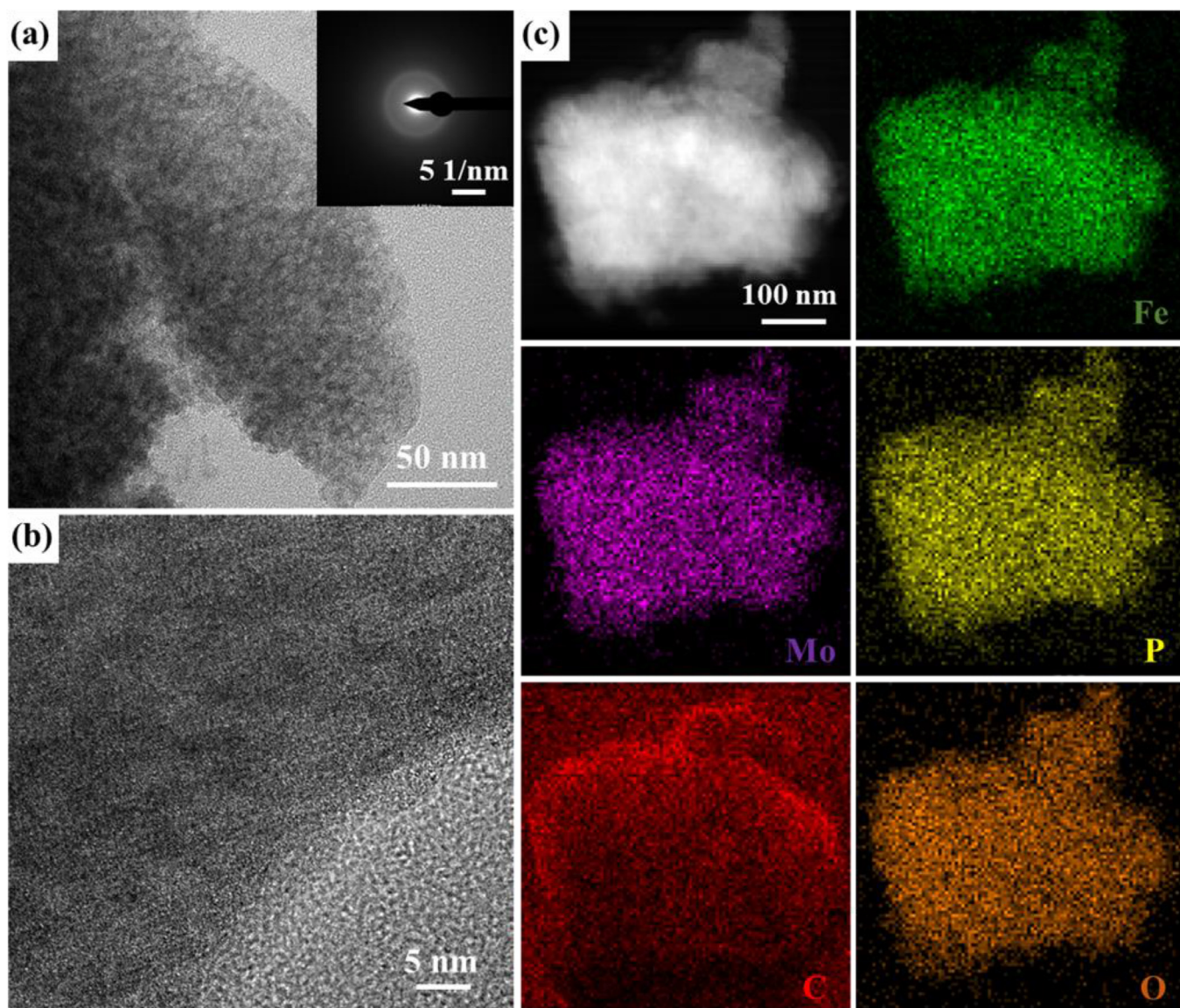

Fig. 5. Structural characterization of the DE@CV Mo4, (a) TEM image, (inset: the corresponding SAED pattern), (b) HRTEM image, (c) HAADF-STEM image and elemental mapping images.
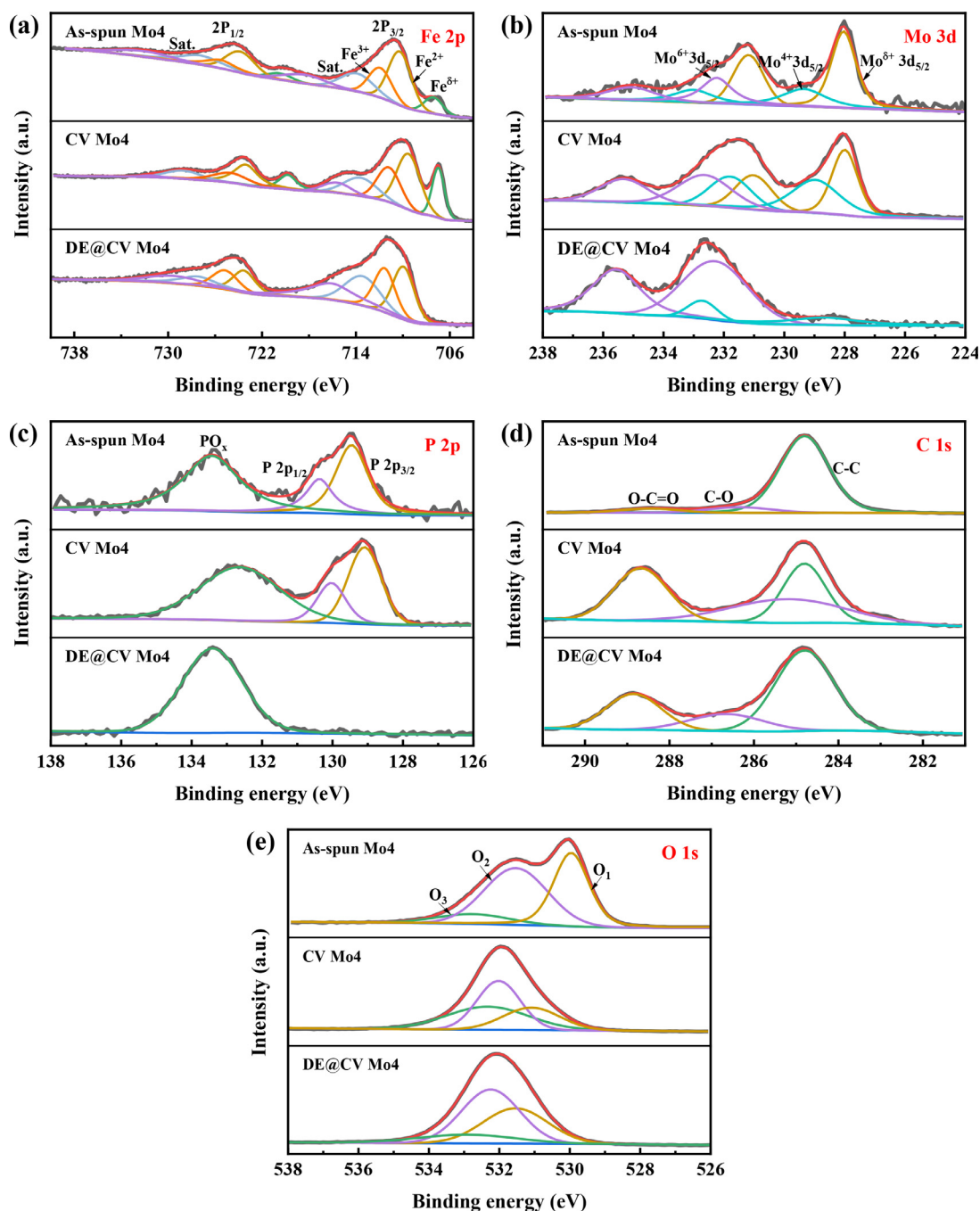
Fig. 6. High-resolution XPS spectra of (a) Fe 2p, (b) Mo 3d, (c) P 2p, (d) C 1s, (e) O 1s of the As-spun Mo4, CV Mo4 and DE@CV Mo4.

the CV Mo4 (Fig. 4b). The EDS line scan of the cross section of the DE@CV Mo4 (as indicated by the white line in Fig. 4c, starting from the circle end) further confirms the hierarchical structure, as a higher concentration of Mo, P, C and O is detected on the 2 μm surface while a higher concentration of Fe is found in the inside (Fig. 4d). In order to identify the atomic structure of the surface layer, HRTEM and SAED analyses of the DE@CV Mo4 were carried out. As shown in Fig. 5a and b, no lattice fringe is observed even at high-resolution TEM image, and no bright diffraction spots from crystallites appear in the SAED pattern (inset of Fig. 5a), indicating the surface layer remains amorphous. It is well known that the amorphous structure can provide a large amount of defects, which can be the reaction sites for absorbing cations and anions to accelerate HER process [50]. Thus, the remained amorphous structure

on the surface is beneficial to the catalytic activity of the DE@CV Mo4. As shown in Fig. 5c, The HAADF image and elemental mapping images manifest the highly homogeneous distribution of Fe, Mo, P, C and O atoms. Such hierarchical sandwich structure provides a great chance to achieve excellent activity and durability of catalysts. The FeMoPC metallic skeleton with high concentration of Fe facilitates efficient electron transfer, while the outer layer with enriched Mo, P, C and O not only provides active reaction sites, but also prevents continuous degradation of the inner matrix. Together with enlarged active surface area of the nanoisland morphology, the DE@CV Mo4 exhibits excellent HER activity and durability.

The electronic structures of the As-spun Mo4, CV Mo4 and DE@CV Mo4 samples were analyzed by XPS. The XPS spectra of
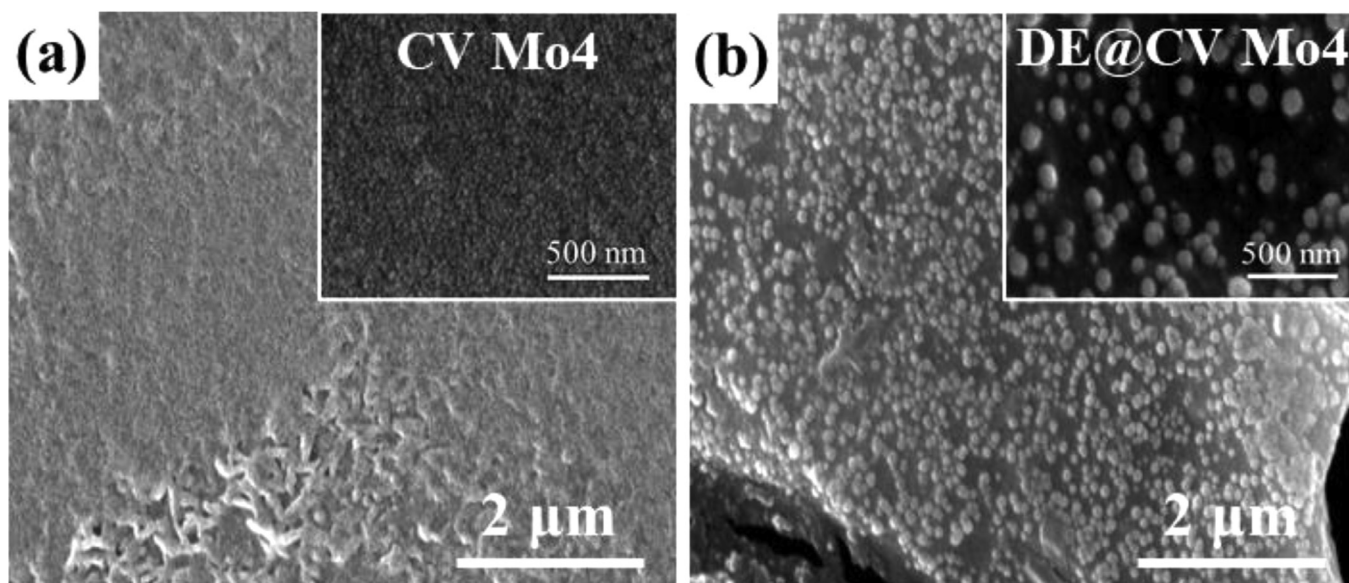
Fig. 7. SEM images of (a) the CV Mo4 and (b) the DE@CVMo4 after long-term HER test.

the elements and binding energy of peaks are shown in Fig. 6 and Tab. S2, respectively. As for the As-spun Mo4, Fig. 6a shows the Fe $2p_{3/2}$ spectrum is deconvoluted into five peaks. The strong peaks at 711.9 eV and 710.3 eV are corresponding to the oxidative Fe^{3+}, Fe^{2+}, respectively. The weak peak at 707.4 eV is indexed to $Fe^{\delta+}$, which is positively shifted from that of metallic Fe (706.8 eV), indicating that Fe of the As-spun Mo4 is partial positively charged $(\delta+)$ [51]. The other peaks at 718.4 eV and 713.9 eV should be assigned to the satellite peaks. Fig. 6b shows that the main Mo $3d_{5/2}$ peaks are deconvoluted into three peaks. The peaks located at 232.3 eV and 229.3 eV are characteristic peaks of Mo^{6+} and Mo^{4+} species, respectively. Likewise, the strong peak at 228.0 eV is close to the position of Mo^0 (227.4-227.8 eV), also meaning the partially charged Mo species $(Mo^{\delta+})$, possibly due to the formation of Mo-P bonds [52]. The P 2p spectrum is also fitted to obtain the exact valence state of P element. As shown in Fig. 6c, the peaks located at 130.4 eV and 129.4 eV are corresponding to the P $2p_{1/2}$ and P $2p_{3/2}$ of M-P (M stands for metallic elements). Apparently, the peak of M-P at 129.4 eV shows negative shift from that of elemental P (130.2 eV), suggesting that P element carries partially negative charge $(\delta-)$ due to partial electron transfer from metals to P [53]. Thus, the formed $P^{\delta-}$ acts as proton-acceptor centers and the formed $Fe^{\delta+}$ or $Mo^{\delta+}$ (or both) acts as the hydride-acceptor, which show strong cooperativity to facilitate the HER process [51]. The peak located at 133.4 eV is indexed to PO_x, which is associated with the oxidation of M-P. Fig. 6d shows the C 1s spectrum has three peaks at 284.8 eV, 285.3 eV and 288.5 eV, which are assigned to C-C, C-O and O-C=O, respectively. Fig. 6e shows the O 1s spectrum can be deconvoluted into three peaks, corresponding to the M-O (530.0 eV) and phosphorus/carbon oxygen (531.5 eV, 532.7 eV).

As for the CV Mo4, Fig. 6a shows the characteristic peaks of Fe 2p spectrum are negatively shifted from that of the As-spun Mo4 and the strength of $Fe^{\delta+}$ is higher. Likewise, the strength of Mo^{4+} and Mo^{6+} is higher (Fig. 6b). It indicates that partially oxidized Fe is reduced, and $Mo^{\delta+}$ or Mo^{4+} (or both) is oxidized during the CV-activation. Fig. 6c shows the peak of M-P is negatively shifted from that of the As-spun Mo4, indicating more electrons are transferred from Fe to P during the CV-activation. Fig. 6d shows that more C changes from zero-valent state to oxidized state on the surface of the CV Mo4 ribbon. Fig. 6e shows that a higher percentage of phos-

phorus/carbon oxygen bond than M-O bond is generated after the CV-activation, which is consistent with the results of C 1s. Based on the electronic structure analyses, the synergetic effect seen in the electrochemically active Fe, Mo, P, C and O species, contributes to the low overpotential of the CV Mo4.

As for the DE@CV Mo4, Fig. 6 shows the characteristic peaks of $Fe^{\delta+}$ and $Mo^{\delta+}$ disappear completely, suggesting the severe oxidation occurred during the dealloying. In addition, the surface metal phosphides completely converted to the acid-resistant phosphates, which not only tailor the surface electronic properties of the catalyst, but also ensure long-term stability of the catalyst [22,54]. The electrical conductivity of the DE@CV Mo4 ribbons is $1.3*10^4$ S•m^{-1}, smaller than that of the As-spun Mo4 ($3.2*10^5$ S m^{-1}), due to a mixture of metallic oxide and metallic phosphate on the surface of the DE@CV Mo4. Based on the results from EDS line scan in Fig. 4d, these oxides and phosphates consist higher concentration of Mo than the inner part. Thus, this layer can prevent the inner metallic skeleton from degradation, leading to the excellent durability of the DE@CV during HER process.

To verify the improved durability by dealloying, the electronic structure and surface morphology of the CV Mo4 and DE@CV Mo4 after long-term HER were compared. As shown in Fig. S6, the XPS of the CV Mo4 shows that the noticeable disappearance of $Fe^{\delta+}$, $Mo^{\delta+}$ and metal phosphides occurs after 10 h HER. As shown in Fig. S7, even after 16 h HER test, the binding energies of Fe, Mo, P, C and O for the DE@CV Mo4 have no obvious change, which confirms its stability. Furthermore, the surface morphology of the CV Mo4 after 10 h HER and DE@CV Mo4 after 16 h HER was compared, and shown in Fig. 7a and b, respectively. A large amount of flower-like, easily exfoliated structures and more refined, granular-like nanoislands caused by the dissolution of metal are observed on the surface of CV Mo4. The flower-like structure allows acidic solution to penetrate into the inner part of the ribbon, thus the sample is oxidized and degraded continuously during long-term HER, resulting in the inferior stability of the CV Mo4 in acidic media. As shown in Fig. 7b, the DE@CV Mo4 after 16 h HER has a large number of particles on the surface. The underlaid matrix is a compact layer, which can better protect the inner part of the ribbon from corrosion than the flower-like structure. This unique structure contributes to the excellent stability of the DE@CV Mo4. Fig. 8 shows that the surface layer of the DE@CV Mo4 is mainly amor-
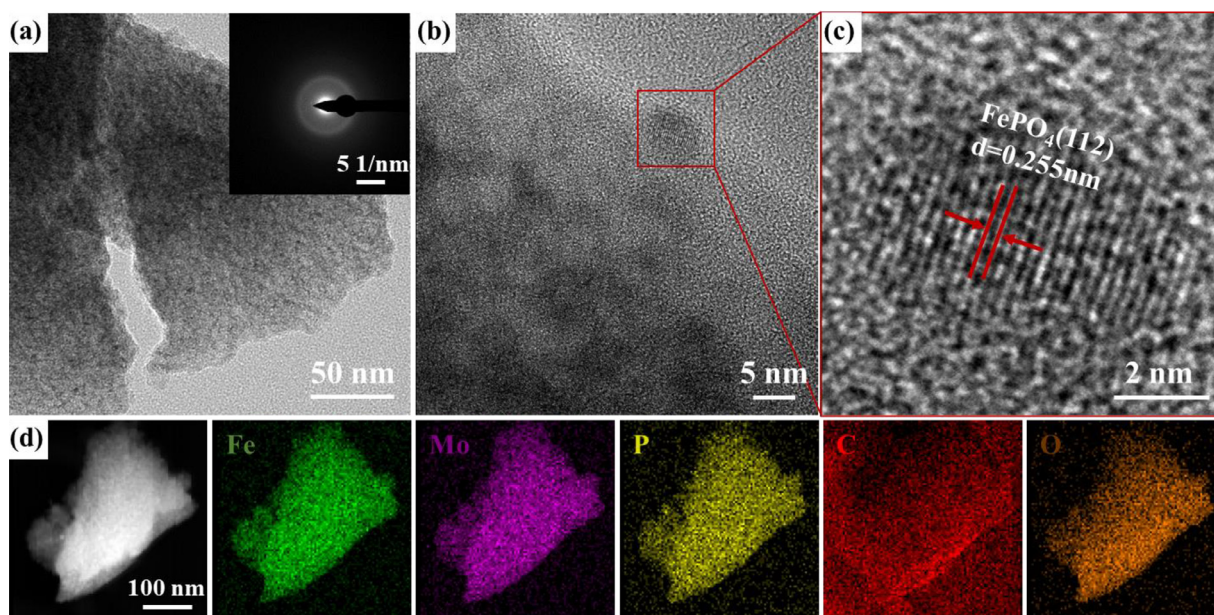
Fig. 8. Structural characterization of the DE@CV Mo4 after 16 h HER test, (a) TEM image, (inset: the corresponding SAED pattern), (b-c) HRTEM images, (d) HAADF-STEM image and elemental mapping images.

phous with a little amount of crystallized $FePO_4$, and all the elements still distribute uniformly after stability testing. It confirms the formation of phosphates that can protect the inner layer from further corrosion. However, the XRD of the DE@CV Mo4 after 16 h test only exhibits a broad diffraction peak (Fig. S8), as it is difficult to detect the small amount of crystalline phase on the surface. The XRD result further confirms the amorphous nature of the major part of the ribbons.

4. Conclusion

In summary, a self-supported, high-efficient and durable FeMoPC amorphous HER catalyst with unique sandwich structure was prepared by a two-step CV activation-dealloying method. It exhibits an overpotential as low as 96 mV@10 mA cm^{-2} with a small Tafel slope of 51mV dec^{-1}, and excellent long-term stability in 0.5 M H_2SO_4 electrolyte. The CV-activation induces formation of nanoislands with remarkably enlarged surface area to boosts the HER reaction. The subsequent dealloying promotes the formation of acid resistant metal phosphate/oxide compact layer, which greatly enhance the durability of catalyst. Besides, the proper combination of Mo and Fe on the amorphous outlayer of the DE@CV Mo4 has the synergetic effect and provides enough reaction sites to enhance the catalytic activity, and the high Fe-containing inner part provides fast electron transport, thus the unique sandwich structure induces an excellent catalyst. This work provides an effective approach to optimize the activity and stability of Fe-based amorphous HER catalysts in acidic electrolyte.

Credit authorship contribution statement

Genmiao Shao: Methodology, Data curation, Investigation, Writing-original draft. **Qianqian Wang**: Supervision, Writing-review & editing. **Fang Miao**: Investigation. **Jiaqi Li**: Investigation. **Yongjie Li**: Investigation. **Baolong Shen**: Conceptualization, Methodology, Funding acquisition, Project administration, Writing-review & editing.

Declaration of Competing Interest

We declare that we do not have any commercial or associative interest that represents a conflict of interest in connection with the work submitted.

Acknowledgements

Supplementary materials

Supplementary material associated with this article can be found, in the online version, at doi:10.1016/j.electacta.2021.138815.

References

[1] N.T. Suen, S.F. Hung, Q. Quan, N. Zhang, Y.J. Xu, H.M. Chen, Electrocatalysis for the oxygen evolution reaction: recent development and future perspectives, Chem. Soc. Rev. 4 (2016) 303–562, doi:10.1039/C6CS00328A.

[2] J. Wang, W. Cui, Q. Liu, Z. Xing, A.M. Asiri, X. Sun, Recent progress in cobalt-based heterogeneous catalysts for electrochemical water splitting, Adv. Mater. 28 (2016) 215–230, doi:10.1002/adma.201502696.

[3] Z. Zhou, X. Li, Q. Li, Y. Zhao, H. Pang, Copper-based materials as highly active electrocatalysts for the oxygen evolution reaction, Mater. Today Chem. 11 (2019) 169–196, doi:10.1016/j.mtchem.2018.10.008.

[4] X. Zou, Y. Zhang, Noble metal-free hydrogen evolution catalysts for water splitting, Chem. Soc. Rev. 44 (2015) 5148–5180, doi:10.1039/C4CS00448E.

[5] C.M. Guio, L.A. Stern, X. Hu, Nanostructured hydrotreating catalysts for electrochemical hydrogen evolution, Chem. Soc. Rev. 43 (2014) 6555–6569, doi:10.1039/c3cs60468c.

[6] D. Strmcnik, P.P. Lopes, B. Genorio, V.R. Stamenkovic, N.M. Markovic, Design principles for hydrogen evolution reaction catalyst materials, Nano Energy 29 (2016) 29–36, doi:10.1016/j.nanoen.2016.04.017.

[7] J. Yu, Y. Guo, S. She, S. Miao, M. Ni, W. Zhou, M. Liu, Z. Shao, Bigger is surprisingly better: agglomerates of larger RuP nanoparticles outperform benchmark Pt nanocatalysts for the hydrogen evolution reaction, Adv. Mater. 30 (2018) 1800047, doi:10.1002/adma.201800047.

[8] M.R. Gao, J.X. Liang, Y.R. Zheng, Y.F. Xu, J. Jiang, Q. Gao, J. Li, S.H. Yu, An efficient molybdenum disulfide/cobalt diselenide hybrid catalyst for electrochemical hydrogen generation, Nat. Commun. 6 (2015) 5982, doi:10.1038/ncomms6982.

[9] Y.C. Hu, Y.Z. Wang, R. Su, C.R. Cao, F. Li, C.W. Sun, Y. Yang, P.F. Guan, D.W. Ding, Z.L. Wang, W.H. Wang, A highly efficient and self-stabilizing metallic-glass cat-

alyst for electrochemical hydrogen generation, Adv. Mater. 28 (2016) 10293–10297, doi:10.1002/adma.201603880.

[10] Z. Jia, T. Yang, L. Sun, Y. Zhao, W. Li, J. Luan, F. Lyu, L.C. Zhang, J.J. Kruzic, J.J. Kai, J.C. Huang, J. Lu, C.T. Liu, A novel multinary intermetallic as an active electrocatalyst for hydrogen evolution, Adv. Mater. 32 (2020) 2000385, doi:10.1002/adma.202000385.

[11] R. Li, X. Liu, R. Wu, J. Wang, Z. Li, K.C. Chan, H. Wang, Y. Wu, Z. Lu, Flexible honeycombed nanoporous/glassy hybrid for efficient electrocatalytic hydrogen generation, Adv. Mater. 31 (2019) 1904989, doi:10.1002/adma.201904989.

[12] C. Wang, J. Jiang, X. Zhou, W. Wang, J. Zuo, Q. Yang, Alternative synthesis of cobalt monophosphide@C core-shell nanocables for electrochemical hydrogen production, J. Power Sources 286 (2015) 464–469, doi:10.1016/j.jpowsour.2015.04.002.

[13] J. Wang, F. Xu, H. Jin, Y. Chen, Y. Wang, Non-noble metal-based carbon composites in hydrogen evolution reaction: fundamentals to applications, Adv. Mater. 29 (2017) 1605838, doi:10.1002/adma.201605838.

[14] B. Cao, G.M. Veith, J.C. Neuefeind, R.R. Adzic, P.G. Khalifah, Mixed close-packed cobalt molybdenum nitrides as non-noble metal electrocatalysts for the hydrogen evolution reaction, J. Am. Chem. Soc. 135 (2013) 19186–19192, doi:10.1021/ja4081056.

[15] Y. Pan, N. Yang, Y. Chen, Y. Lin, Y. Li, Y. Liu, C. Liu, Nickel phosphide nanoparticles-nitrogen-doped graphene hybrid as an efficient catalyst for enhanced hydrogen evolution activity, J. Power Sources 297 (2015) 45–52, doi:10.1016/j.jpowsour.2015.07.077.

[16] J. Wang, G. Wang, S. Miao, J. Li, X. Bao, Graphene-supported iron-based nanoparticles encapsulated in nitrogen-doped carbon as a synergistic catalyst for hydrogen evolution and oxygen reduction reactions, Faraday Discuss 176 (2014) 135–151, doi:10.1039/c4fd00123k.

[17] M. Baek, G.W. Kim, T. Park, K. Yong, NiMoFe and NiMoFeP as complementary electrocatalysts for efficient overall water splitting and their application in PV-electrolysis with STH 12.3, Small 15 (2019) 1905501, doi:10.1002/smll.201905501.

[18] W. Gu, L. Gan, X. Zhang, E. Wang, J. Wang, Theoretical designing and experimental fabricating unique quadruple multimetallic phosphides with remarkable hydrogen evolution performance, Nano Energy 34 (2017) 421–427, doi:10.1016/j.nanoen.2017.02.049.

[19] J. Xu, J. Li, D. Xiong, B. Zhang, Y. Liu, K.H. Wu, I. Amorim, W. Li, L. Liu, Trends in activity for the oxygen evolution reaction on transition metal (M = Fe, Co, Ni) phosphide pre-catalysts, Chem. Sci. 9 (2018) 3470–3476, doi:10.1039/c7sc05033j.

[20] G.B. Darband, M. Aliofkhazraei, S. Hyun, A.S. Rouhaghdam, S. Shanmugam, Electrodeposited NiCoP hierarchical nanostructure as a cost-effective and durable electrocatalyst with superior activity for bifunctional water splitting, J. Power Sources 429 (2019) 156–167, doi:10.1016/j.jpowsour.2019.04.050.

[21] Y. Tan, H. Wang, P. Liu, C. Cheng, F. Zhu, A. Hirata, M. Chen, 3D nanoporous metal phosphides toward high-efficiency electrochemical hydrogen production, Adv. Mater. 28 (2016) 2951–2955, doi:10.1002/adma.201505875.

[22] X. Zhang, J. Ji, Q. Yang, L. Zhao, Q. Yuan, Y. Hao, P. Jin, L. Feng, Phosphate doped ultrathin FeP nanosheets as efficient electrocatalysts for the hydrogen evolution reaction in acid media, ChemCatChem 11 (2019) 2484–2489, doi:10.1002/cctc.201900256.

[23] Z. Ma, L R., M. Wang, H. Meng, X.Q.Bao F.Zhang, B. Tang, X. Wang, Self-supported porous Ni-Fe-P composite as an efficient electrocatalyst for hydrogen evolution reaction in both acidic and alkaline medium, Electrochim. Acta 219 (2016) 194–203, doi:10.1016/j.electacta.2016.10.004.

[24] D. Kong, J.J. Cha, H. Wang, H.R. Lee, Y. Cui, First-row transition metal dichalcogenide catalysts for hydrogen evolution reaction, Energy Environ. Sci. 6 (2013) 3553, doi:10.1039/c3ee42413h.

[25] B. Song, K. Li, Y. Yin, T. Wu, L. Dang, M. Cabán-Acevedo, J. Han, T. Gao, X. Wang, Z. Zhang, J.R. Schmidt, P. Xu, S. Jin, Tuning mixed nickel iron phosphosulfide nanosheet electrocatalysts for enhanced hydrogen and oxygen evolution, ACS Catalysis 7 (2017) 8549–8557, doi:10.1021/acscatal.7b02575.

[26] D. Friebel, M.W. Louie, M. Bajdich, K.E. Sanwald, Y. Cai, A.M. Wise, M.J. Cheng, D. Sokaras, T.C. Weng, R. Alonso-Mori, R.C. Davis, J.R. Bargar, J.K. Norskov, A. Nilsson, A.T. Bell, Identification of highly active Fe sites in (Ni,Fe)OOH for electrocatalytic water splitting, J. Am. Chem. Soc. 137 (2015) 1305–1313, doi:10.1021/ja511559d.

[27] F. Hu, S. Zhu, S. Chen, Y. Li, L. Ma, T. Wu, Y. Zhang, C. Wang, C. Liu, X. Yang, L. Song, X. Yang, Y. Xiong, Amorphous metallic NiFeP: a conductive bulk material achieving high activity for oxygen evolution reaction in both alkaline and acidic media, Adv. Mater. 29 (2017) 1606570, doi:10.1002/adma.201606570.

[28] J.M.V. Nsanzimana, Y. Peng, Y.Y. Xu, L. Thia, C. Wang, B.Y. Xia, X. Wang, An efficient and earth-abundant oxygen-evolving electrocatalyst based on amorphous metal borides, Adv. Energy. Mater. 8 (2018) 1701475, doi:10.1002/aenm.201701475.

[29] J. Li, G. Doubek, L.M. Brown, A. Taylor, Recent advances in metallic glass nanostructures: synthesis strategies and electrocatalytic applications, Adv. Mater. 31 (2019) 1802120, doi:10.1002/adma.201802120.

[30] S. Jiang, L. Zhu, Z. Yang, Y. Wang, Enhanced electrocatalytic performance of FeNiCoP amorphous alloys as oxygen-evolving catalysts for electrolytic water splitting application, Electrochim. Acta 368 (2021) 137618, doi:10.1016/j.electacta.2020.137618.

[31] A. Bergmann, E. Martinez-Moreno, D. Teschner, P. Chernev, M. Gliech, J.F. de Araujo, T. Reier, H. Dau, P. Strasser, Reversible amorphization and the catalytically active state of crystalline Co$_3$O$_4$ during oxygen evolution, Nat. Commun. 6 (2015) 8625, doi:10.1038/ncomms9625.

[32] A. Indra, P.W. Menezes, N.R. Sahraie, A. Bergmann, C. Das, M. Tallarida, D. Schmeisser, P. Strasser, M. Driess, Unification of catalytic water oxidation and oxygen reduction reactions: amorphous beat crystalline cobalt iron oxides, J. Am. Chem. Soc. 136 (2014) 17530–17536, doi:10.1021/ja509348t.

[33] Y. Tan, F. Zhu, H. Wang, Y. Tian, A. Hirata, T. Fujita, M. Chen, Noble-metal-free metallic glass as a highly active and stable bifunctional electrocatalyst for water splitting, Adv. Mater. Interfaces 4 (2017) 1601086, doi:10.1002/admi.201601086.

[34] J. Masa, P. Weide, D. Peeters, I. Sinev, W. Xia, Z.Y. Sun, C. Somsen, M. Muhler, W. Schuhmann, Amorphous cobalt boride (Co$_2$B) as a highly efficient non-precious catalyst for electrochemical water splitting: oxygen and hydrogen evolution, Adv. Energy. Mater. 6 (2016) 1502313, doi:10.1002/aenm.201502313.

[35] H. Sun, Z. Yan, F. Liu, W. Xu, F. Cheng, J. Chen, Self-supported transition-metal-based electrocatalysts for hydrogen and oxygen evolution, Adv. Mater. 32 (2020) 1806326, doi:10.1002/adma.201806326.

[36] S. Ju, J. Feng, P. Zou, W. Xu, S. Wang, W. Gao, H.J. Qiu, J. Huo, J.Q. Wang, A robust self-stabilized electrode based on Al-based metallic glasses for a highly efficient hydrogen evolution reaction, J. Mater. Chem. A 8 (2020) 3246–3251, doi:10.1039/c9ta11867e.

[37] Y. Yao, N. Mahmood, L. Pan, G. Shen, R. Zhang, R. Gao, F. Aleem, Y X., Z X., Z J.J., Iron phosphide encapsulated in P-doped graphitic carbon as efficient and stable electrocatalyst for hydrogen and oxygen evolution reactions, Nanoscale 10 (2018) 21327–21334, doi:10.1039/C8NR06752J.

[38] F. Zhang, J. Wu, W. Jiang, Q. Hu, B. Zhang, New and efficient electrocatalyst for hydrogen production from water splitting: inexpensive, robust metallic glassy ribbons based on iron and cobalt, ACS Appl. Mater. Interfaces 9 (2017) 31340–31344, doi:10.1021/acsami.7b09222.

[39] K. Wu, Y. Meng, X. Li, J. Ma, P. Zhang, W. Li, H.J. Lin, Improved alkaline hydrogen evolution performance of a Fe$_{78}$Si$_9$B$_{13}$ metallic glass electrocatalyst by ultrasonic vibrations, Intermetallics 125 (2020) 106820, doi:10.1016/j.intermet.2020.106820.

[40] A.L. Goff, V. Artero, B. Jousselme, P.D. Tran, N. Guillet, From hydrogenases to noble metal free catalytic nanomaterials for H$_2$ production and update, Science 326 (2009) 1384–1387, doi:10.1126/science.1179773.

[41] B.E. Conway, G. Jerkiewicz, Relation of energies and coverages of underpotential and overpotential deposited H at Pt and other metals to the volcano curve for cathodic H$_2$ evolution kinetics, Electrochim. Acta 45 (2000) 4075–4083, doi:10.1016/S0013-4686(00)00523-5.

[42] Y. Zhu, Y. Pan, W. Dai, T. Lu, Dealloying generation of oxygen vacancies in the amorphous nanoporous Ni-Mo-O for superior electrocatalytic hydrogen generation, ACS Appl. Energy Mater. 3 (2020) 1319–1327, doi:10.1021/acsaem.9b01563.

[43] X. Wang, G. She, L. Mu, W. Shi, Amorphous Co-Mo-P-O bifunctional electrocatalyst via facile electrodeposition for overall water splitting, ACS Sustain. Chem. Eng. 8 (2020) 2835–2842, doi:10.1021/acssuschemeng.9b06129.

[44] Z.W. Seh, J. Kibsgaard, C.F. Dickens, I. Chorkendorff, J.K. Norskov, T.F. Jaramillo, Combining theory and experiment in electrocatalysis: insights into materials design, Science 355 (2017) eaad4998, doi:10.1126/science.aad4998.

[45] R. Jiang, Z. Cui, W. Xu, S. Zhu, Y. Liang, Z. Li, S. Wu, C. Chang, A. Inoue, Highly efficient amorphous np-PdFePC catalyst for hydrogen evolution reaction, Electrochim. Acta 328 (2019) 135082, doi:10.1016/j.electacta.2019.135082.

[46] F. Hu, H. Wang, Y. Zhang, X. Shen, G. Zhang, Y. Pan, J.T. Miller, K. Wang, S. Zhu, X. Yang, C. Wang, X. Wu, Y. Xiong, Z. Peng, Designing highly efficient and long-term durable electrocatalyst for oxygen evolution by coupling B and P into amorphous porous NiFe-based material, Small 15 (2019) 1901020, doi:10.1002/smll.201901020.

[47] C. Yang, R. Zhao, H. Xiang, J. Wu, W. Zhong, W. Li, Q. Zhang, N. Yang, X. Li, Ni-activated transition metal carbides for efficient hydrogen evolution in acidic and alkaline solutions, Adv. Energy. Mater. 10 (2020) 2002260, doi:10.1002/aenm.202002260.

[48] Z.J. Wang, M.X. Li, J.H. Yu, X.B. Ge, Y.H. Liu, W.H. Wang, Low-iridium-content irnita metallic glass films as intrinsically active catalysts for hydrogen evolution reaction, Adv. Mater. 32 (2020) 1906384, doi:10.1002/adma.201906384.

[49] H. Zhang, P. An, W. Zhou, B.Y. Guan, P. Zhang, J. Dong, X.W. Lou, Dynamic traction of lattice-confined platinum atoms into mesoporous carbon matrix for hydrogen evolution reaction, Sci. Adv. 4 (2018) eaao6657, doi:10.1126/sciadv.aao6657.

[50] S. Anantharaj, S. Noda, Amorphous catalysts and electrochemical water splitting: an untold story of harmony, Small 16 (2019) 1905779, doi:10.1002/smll.201905779.

[51] Y. Liang, Q. Liu, A.M. Asiri, X. Sun, Y. Luo, Self-supported FeP nanorod arrays: a cost-effective 3d hydrogen evolution cathode with high catalytic activity, ACS Catalysis 4 (2014) 4065–4069, doi:10.1021/cs501106g.

[52] D.C. Phillips, S.J. Sawhill, R. Self, M.E. Bussell, Synthesis, characterization, and hydrodesulfurization properties of silica-supported molybdenum phosphide catalysts, J. Catal. 207 (2002) 266–273, doi:10.1006/jcat.2002.3524.

[53] M. Wang, R. Zhao, X. Li, X. Zhao, L. Jiang, Three-dimensional assembly of iron phosphide nanosheets: synthesis and enhanced catalytic activity for hydrogen evolution reaction, ChemNanoMat 5 (2019) 593–598, doi:10.1002/cnma.201800633.

[54] H. Zhao, Z.Y. Yuan, Insights into transition metal phosphate materials for efficient electrocatalysis, ChemCatChem 12 (2020) 3797–3810, doi:10.1002/cctc.202000360.